






 Cite this: *RSC Adv.*, 2021, 11, 16490

# Solvothermal synthesis of poly(acrylic acid) decorated magnetic molybdenum disulfide nanosheets for highly-efficient adsorption of cationic dyes from aqueous solutions†

 Li Lei,  Zhuo Peng,  Ting Liang,  Hai-Rong Yu \* and Chang-Jing Cheng \*

Herein we report solvothermal synthesis of poly(acrylic acid) (PAA) decorated magnetic molybdenum disulfide nanosheets (MMoS<sub>2</sub>/PAA) for highly efficient adsorption of three cationic dyes of basic fuchsin (BF), methylene blue (MB), and crystal violet (CV) from aqueous solutions. The synthesized MMoS<sub>2</sub>/PAA was characterized by several techniques including transmission electron microscopy (TEM), Fourier transform-infrared spectroscopy (FT-IR), X-ray photoelectron spectroscopy (XPS), thermogravimetric analysis (TGA), vibrating sample magnetometry (VSM), and dynamic light scattering (DLS). Due to the strong electrostatic interaction between cationic dyes and the anionic nanosheet surface, the obtained MMoS<sub>2</sub>/PAA showed ultrafast adsorption of BF, MB and CV within 2 min with high adsorption capacities of 886.1, 709.0, and 633.6 mg g<sup>-1</sup>, respectively, much higher than those materials reported recently. PAA molecules bound on the nanosheets played a crucial role in significantly enhancing the dye adsorption. The adsorption kinetics and isotherms of three dyes onto the MMoS<sub>2</sub>/PAA were well described by the pseudo-second-order kinetic and the Langmuir models. Moreover, the MMoS<sub>2</sub>/PAA also exhibited high removal efficiencies for various mixed-dye solutions. Besides, such a functional nanomaterial could be effectively recovered from dye solutions under an external magnetic field and reused for dye adsorption without compromising on its performance indicating it can serve as an excellent adsorbent for effective removal of a variety of cationic organic pollutants from industrial effluents.

Received 26th February 2021

Accepted 28th April 2021

DOI: 10.1039/d1ra01548f

[rsc.li/rsc-advances](https://rsc.li/rsc-advances)

## 1. Introduction

Organic dyes are widely used in printing, textiles, paint, pigment and many other significant industries. Dye effluents discharged from numerous dye-utilizing industries have posed a serious threat to human beings and marine environments.<sup>1,2</sup> The presence of dyes in water reduces the light penetration and lowers oxygen gas solubility, thus decreasing the photosynthetic efficiency of aquatic plants. Moreover, most dyes are highly toxic and can have teratogenic, carcinogenic and mutagenic effects on aquatic life and humans even at a very low concentration.<sup>3,4</sup> Therefore, effective removal of dye contaminants prior to discharge into the water environment is of great

importance. Currently various biological, chemical and/or physical technologies such as biodegradation, chemical oxidation, ion exchange, membrane filtration and adsorption have been used for eliminating dye pollutants from environmental wastewater.<sup>1-6</sup> Among them, adsorption is regarded as the most effective technique to remove dye contaminants from water since its inexpensiveness, high efficiency, wide adaptability and convenient operation.<sup>3-7</sup> The key of this method is developing high-performance adsorbents.

Two-dimensional (2D) laminar materials have recently attracted considerable attentions as promising adsorbents for pollutant treatment due to their unique properties of large specific surface area, high chemical stability, and low production cost.<sup>8,9</sup> Molybdenum disulfide (MoS<sub>2</sub>) nanosheets and their composites, as newly emerging 2D layered materials have been intensively studied for eliminating varieties of organic and inorganic pollutants from water.<sup>10-14</sup> However, recovering those nanomaterials from aqueous solutions is time-consuming and expensive owing to involvement of complex filtration or/and centrifugation operations, thus hampering their practical applications. Loading certain amount of superparamagnetic Fe<sub>3</sub>O<sub>4</sub> nanoparticles (NPs) on the surface endows them convenient separability from contaminated water under an external

College of Chemistry and Environment, Southwest Minzu University, No. 16 South Section 4, Yihuan Road, Chengdu, Sichuan, 610041, P. R. China. E-mail: yuhr@swun.edu.cn; chengcj@swun.edu.cn

† Electronic supplementary information (ESI) available: High-resolution XPS spectra of Mo 3d and S 2p in MoS<sub>2</sub> and MMoS<sub>2</sub>/PAA-80 samples; digital photographs of MMoS<sub>2</sub>/PAA-80 and MMoS<sub>2</sub> aqueous dispersions after keeping different times; zeta potentials of MMoS<sub>2</sub> and MMoS<sub>2</sub>/PAA-80; fitting of pseudo-first-order kinetic model of BF, MB, and CV adsorption onto MMoS<sub>2</sub>/PAA-80; molecular structures of methylene blue (MB), basic fuchsin (BF), and crystal violet (CV); effect of temperature on the adsorption of BF, MB, and CV onto MMoS<sub>2</sub>/PAA-80. See DOI: 10.1039/d1ra01548f



magnetic field (EMF) seems feasible to solve this problem. However, introducing  $\text{Fe}_3\text{O}_4$  NPs inevitably reduces active adsorption sites on their surface, thus lowering its equilibrium adsorption capacity for pollutants.<sup>15,16</sup> Through surface decoration using polymers with rich active groups will dramatically enhance their uptakes for organic dyes.

In this work, poly(acrylic acid) (PAA) with plentiful of anionic carboxylic groups ( $-\text{COO}^-$ ) that have high affinity to cationic dyes, was utilized to decorate  $\text{Fe}_3\text{O}_4$  NPs-loaded  $\text{MoS}_2$  nano-sheets for synthesizing  $\text{MMoS}_2/\text{PAA}$  nanocomposite. The synthesized  $\text{MMoS}_2/\text{PAA}$  showed high adsorption capacities for three typical cationic dyes of basic fuchsin (BF), methylene blue (MB), and crystal violet (CV). As shown in Fig. 1a,  $\text{MoS}_2$  nano-sheets with relative large specific surface area were first synthesized by versatile hydrothermal method.<sup>17</sup> Then super-paramagnetic  $\text{Fe}_3\text{O}_4$  NPs and poly(acrylic acid) (PAA) functional polymers were simultaneously introduced on the  $\text{MoS}_2$  surface by simple solvothermal reaction, thus causing the formation of

$\text{MMoS}_2/\text{PAA}$ . The resulted  $\text{MMoS}_2/\text{PAA}$  was characterized by several techniques including transmission electron microscope (TEM), Fourier transform-infrared spectroscopy (FT-IR), X-ray photoelectron spectroscopy (XPS), thermogravimetric analysis (TGA), vibrating sample magnetometry (VSM), and dynamic light scattering (DLS) instrument. Thanks to strong electrostatic interaction between cationic dyes and the anionic  $-\text{COO}^-$  groups in PAA molecules, the  $\text{MMoS}_2/\text{PAA}$  showed ultrafast adsorption of BF, MB and CV within 2 min with high adsorption capacities of 886.1, 709.0, and 633.6  $\text{mg g}^{-1}$ , respectively, comparable and even higher than those materials reported previously (Table 1).<sup>4,10,11,15,18–23</sup> PAA molecules on the  $\text{MoS}_2$  played a crucial role in significantly enhancing the adsorption of cationic dyes. The adsorption behaviors were fitted well with the pseudo-second-order kinetic and the Langmuir models. The batch adsorption experiments with the effects of parameters like solution pH, contact time, initial dye concentrations and temperature on the adsorption were optimized for dye adsorption. Moreover,

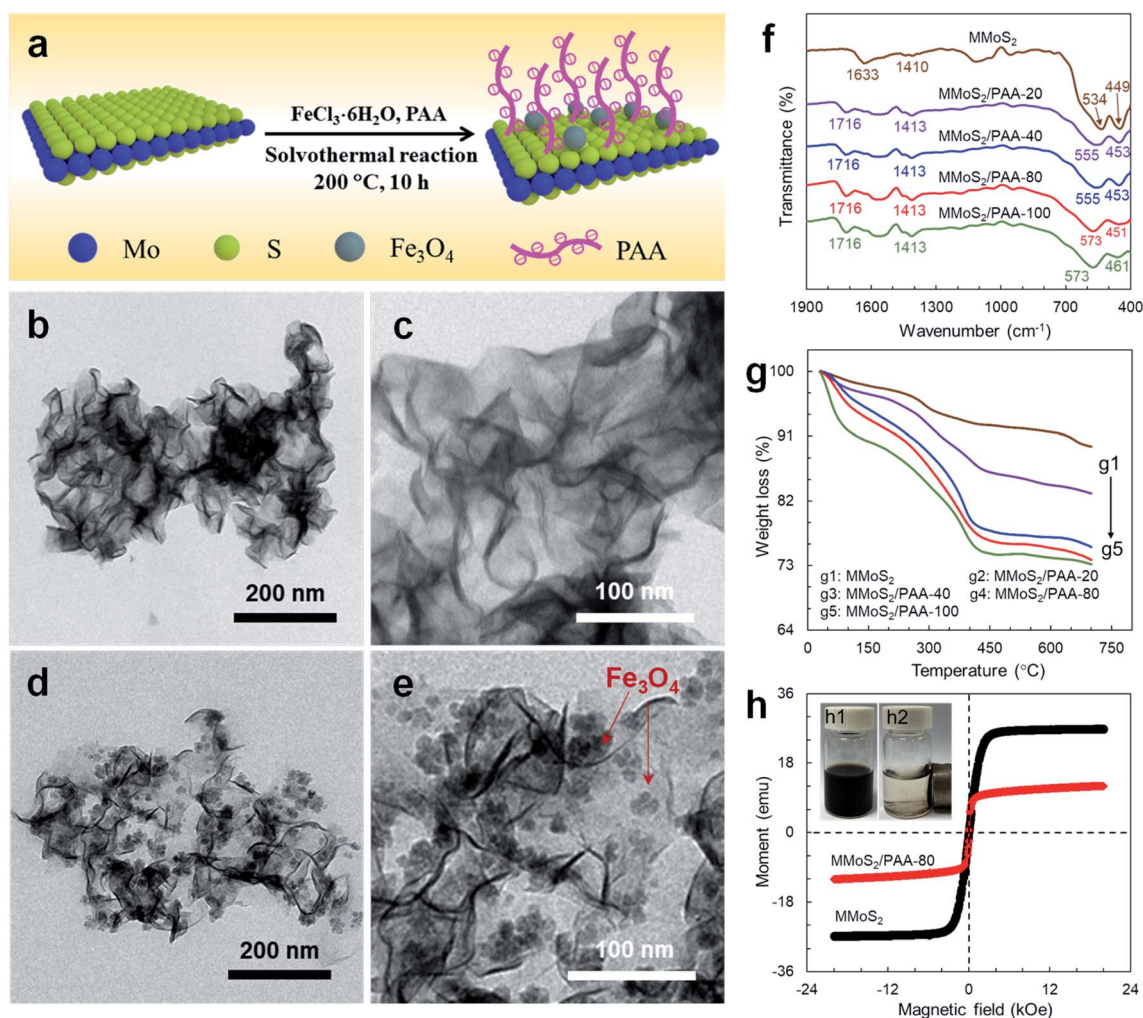


Fig. 1 (a) Schematic illustration of the synthesis of  $\text{MMoS}_2/\text{PAA}$ ; typical TEM images of (b and c)  $\text{MoS}_2$  and (d and e)  $\text{MMoS}_2/\text{PAA-80}$ ; FT-IR spectra (f) and TGA curves (g) of  $\text{MMoS}_2$ ,  $\text{MMoS}_2/\text{PAA-20}$ ,  $\text{MMoS}_2/\text{PAA-40}$ ,  $\text{MMoS}_2/\text{PAA-80}$ , and  $\text{MMoS}_2/\text{PAA-100}$ ; (h) magnetic hysteresis curves of  $\text{MoS}_2$  and  $\text{MMoS}_2/\text{PAA-80}$ . The inset showed the digital photographs of  $\text{MMoS}_2/\text{PAA-80}$  aqueous dispersion before (h1) and after (h2) magnetic separation.

Table 1 Comparison of dye adsorption capacity by various adsorbents

Adsorbent	Dye	$q_e$ (mg g <sup>-1</sup> )	Ref.
Fe <sub>3</sub> O <sub>4</sub> /chitosan/graphene	MB	81.6	4
MoS <sub>2</sub> /graphene on cellulose paper	MB	485.4	10
Ultrathin MoS <sub>2</sub> nanosheets	MB	146.4	11
Fe <sub>3</sub> O <sub>4</sub> decorated MoS <sub>2</sub> nanosheets	Congo	71.0	15
NH <sub>2</sub> -modified titanate nanotubes	Remazol blue R	435.6	18
PSSMA-modified Fe <sub>3</sub> O <sub>4</sub> NPs	MB	52.2	19
PAA-functionalized magnetic GO	MB	291.0	20
M3D-PAA-CCN	MB	332.0	21
Fe <sub>3</sub> O <sub>4</sub> /activated carbon	Rhodamine B	182.5	22
	Methyl orange	150.4	22
Chitosan/heulandite/Fe <sub>3</sub> O <sub>4</sub>	MB	45.1	23
	Methyl orange	149.2	23
MMoS <sub>2</sub> /PAA	BF	886.1	This work
	MB	709.0	
	CV	633.6	

the MMoS<sub>2</sub>/PAA also demonstrated high removal efficiency for various mixed dye solutions and excellent regenerability. Such a functional nanocomposite with ultrafast adsorption rate and high adsorption capacities for cationic dyes is promising to become an excellent adsorbent for removing various cationic organic pollutants from industrial effluents.

## 2. Experimental section

### 2.1 Chemical materials

Sodium molybdate dihydrate (Na<sub>2</sub>Mo<sub>4</sub>·2H<sub>2</sub>O, ≥99.0%) and thioacetamide (C<sub>2</sub>H<sub>5</sub>NS, ≥99.0%) were purchased from Aladdin Chemicals (Shanghai, China). Poly(acrylic acid) (PAA,  $M_w = 1800$ , ≥99.0%) was obtained from Sigma-Aldrich Chemicals (Shanghai, China). Iron(III) chloride hexahydrate (FeCl<sub>3</sub>·6H<sub>2</sub>O, ≥99%), sodium acetate anhydrous (CH<sub>3</sub>COONa, ≥99.0%), basic fuchsin (BF, ≥99.0%), methylene blue (MB, ≥99.0%), and crystal violet (CV, ≥99.0%) were bought from Kelong Chemicals (Chengdu, China). All other chemicals were of analytical grade (≥99.5%), purchased from Chengdu Kelong Chemicals and used as received. Deionized water (18.2 MΩ, 25 °C) from a Milli-Q plus purification system (Millipore) was used throughout the experiments.

### 2.2 Synthesis of MoS<sub>2</sub> nanosheets

MoS<sub>2</sub> nanosheets were synthesized by a versatile hydrothermal reaction.<sup>17</sup> Briefly, 0.3 g of Na<sub>2</sub>Mo<sub>4</sub>·2H<sub>2</sub>O and 0.6 g of C<sub>2</sub>H<sub>5</sub>NS were dissolved in 40 mL water by sonication for 30 min. Then the obtained solution was transferred into a 100 mL Teflon-lined stainless-steel autoclave and reacted at 220 °C for 24 h. After natural cooling, the black precipitate was separated by centrifugation at 8500 rpm for 15 min and then washed with water several times, and finally dispersed in 20 mL water for subsequent use.

### 2.3 Synthesis of MMoS<sub>2</sub>/PAA

PAA-bound magnetic MoS<sub>2</sub> nanosheets (MMoS<sub>2</sub>/PAA) were synthesized according to the ref. 17 with some modification. In

brief, 15 mL of MoS<sub>2</sub> aqueous dispersion (~100 mg MoS<sub>2</sub>) was mixed with 30 mL water/ethanol (v/v = 1 : 2) for 1 h by ultrasonication. Then 0.5 g of FeCl<sub>3</sub>·6H<sub>2</sub>O, 0.75 g of CH<sub>3</sub>COONa and some amount of PAA (0, 20, 40, 80, and 100 mg) were added under stirring for 30 min. After that, the mixture was transferred into 100 mL Teflon-lined stainless-steel autoclave and heated at 200 °C for 10 h. After natural cooling, the black precipitates were collected with a magnet and washed with water several times, and then dispersed in 20 mL water (denoted as MMoS<sub>2</sub>, MMoS<sub>2</sub>/PAA-20, MMoS<sub>2</sub>/PAA-40, MMoS<sub>2</sub>/PAA-80, and MMoS<sub>2</sub>/PAA-100, respectively) for the subsequent adsorption experiments. To conduct the contrast trials, PAA-modified magnetic NPs sample (Fe<sub>3</sub>O<sub>4</sub>/PAA-100) was synthesized with the same method using 100 mg PAA while without addition of MoS<sub>2</sub> during the solvothermal reaction.

### 2.4 Characterization

Transmission Electron Microscope (TEM) images were obtained with a JEM-2010 microscope (JEOL, Japan) at an accelerating voltage of 120 kV. The samples were prepared by drop-casting a dilute solution of particles onto carbon-coated copper grids, followed by air drying. FT-IR spectra were recorded on an IR 200 spectrometer (Thermo Nicolet, USA) using KBr pellets. X-Ray photoelectron spectroscopy (XPS) was performed on a Thermo Fisher ESCALAB Xi+. Thermogravimetric analysis (TGA) was performed on a Mettler TGA/SDTA851e° instrument (Switzerland) at a heating rate of 5 °C min<sup>-1</sup> from 30 to 700 °C under N<sub>2</sub> atmosphere. Magnetic property was measured by vibrating sample magnetometry (VSM) on a model 2000 physical property measurement system (Quantum Design) at room temperature. Zeta potentials of samples were determined on a dynamic light scattering (DLS) instrument (Zetasizer Nano-ZS, Malvern Instruments, UK).

### 2.5 Batch adsorption experiments

Typically, 10 mg of MoS<sub>2</sub> nanocomposites was added in 30 mL aqueous solutions contained BF, MB, and CV with desired concentrations and pH values in glass vials. The initial pH

values of solutions were regulated by adding negligible volume of 0.1 M NaOH and/or HCl solution. Then the solid-liquid mixtures were shaken in a thermostatic shaker (80 rpm) at a desired temperature for certain time. To confirm that PAA bound on the MMoS<sub>2</sub> played a significant role in adsorption of three cationic dyes, the MMoS<sub>2</sub>/PAA serials samples synthesized with different dosages of PAA during the solvothermal process (MMoS<sub>2</sub>, MMoS<sub>2</sub>/PAA-20, MMoS<sub>2</sub>/PAA-40, MMoS<sub>2</sub>/PAA-80, and MMoS<sub>2</sub>/PAA-100) were used for dye adsorption. To study the effect of initial dye concentration on the adsorption and adsorption isotherms, the concentrations were varied from 50 to 600 mg L<sup>-1</sup> for MB and CV, and from 50 to 700 mg L<sup>-1</sup> for BF. To probe the influence of contact time on the adsorption and adsorption dynamics, the contact time between adsorbents and dyes changed from 0 to 20 min. The dye-saturated materials were collected from solutions with a magnet, and the dye concentrations before and after adsorption were measured on a UV-vis spectrophotometer (TU-1950, Persee, Beijing, China) at the absorbance of 540, 664 and 590 nm for BF MB, and CV, respectively. The used adsorbents were regenerated by washing thrice with NaOH/ethanol solution (0.1 M) and reused for dye adsorption. The adsorption capacity,  $q_e$  (mg g<sup>-1</sup>) and removal efficiency (%) of dyes onto adsorbents were calculated from the following equations:

$$q_e = \frac{(C_0 - C_e) \times V}{m} \quad (1)$$

$$\text{Removal}(\%) = \frac{C_0 - C_e}{C_0} \times 100\% \quad (2)$$

where  $C_0$  and  $C_e$  (mg L<sup>-1</sup>) are the initial and equilibrium concentrations of dyes in solutions, respectively.  $V$  (L) is the volume of dye solutions, and  $m$  (g) is the mass of adsorbents. All the adsorption experiments were performed at least thrice.

### 3. Results and discussion

#### 3.1 Materials characterizations

The morphologies and microstructures of materials were observed by TEM. As observed in Fig. 1b and c, MoS<sub>2</sub> has a 2D wrinkled and layered microstructure. After solvothermal reaction, multiple black Fe<sub>3</sub>O<sub>4</sub> NPs with size range of 20–50 nm were loaded on the MoS<sub>2</sub> surface (Fig. 1d and e), endowing convenient separability of MoS<sub>2</sub> nanosheets from contaminated aqueous solutions under an EMF. Loh and coworkers reported one kind of edge-oriented MoS<sub>2</sub> nanosheet-like films that exhibited weak magnetism (~1–2 emu g<sup>-1</sup>) and 2.5% magnetoresistance effects with a Curie temperature of 685 K.<sup>24</sup> The metal oxides or sulfides film with a high density of edge spins could give rise to interesting magnetic phenomena even though the bulk material is nonmagnetic. The MoS<sub>2</sub> thin films prepared by thermal evaporation of the single-source precursor tetrakis(diethyl-aminodithiocarbamate)molybdate(IV) owned the rhombohedral or hexagonal edges. In this work the MoS<sub>2</sub> nanosheets were synthesized by hydrothermal reaction, and demonstrated significantly different 2D wrinkled and layered microstructure, which is consistent with those previous

reports.<sup>17,25</sup> The successful binding of PAA on the magnetic MoS<sub>2</sub> (MMoS<sub>2</sub>) surface was confirmed by FT-IR spectrum. Fig. 1f shows the FT-IR spectra of MMoS<sub>2</sub> before and after binding of PAA. MMoS<sub>2</sub> is composed of MoS<sub>2</sub> and Fe<sub>3</sub>O<sub>4</sub>. As observed in Fig. 1f, the strong band at around 1633 cm<sup>-1</sup> is attributed to the bending vibration of adsorbed water molecules on the MoS<sub>2</sub> surface,<sup>26</sup> the adsorption band at 1410 cm<sup>-1</sup> is related to the C–N groups from the C<sub>2</sub>H<sub>5</sub>NS used in the synthesis,<sup>27</sup> and the characteristic peak at 449 cm<sup>-1</sup> is attributable to the Mo–S bond from the MoS<sub>2</sub>.<sup>26</sup> Besides, the peak at 534 cm<sup>-1</sup> is due to the Fe–O stretching vibration from Fe<sub>3</sub>O<sub>4</sub> NPs,<sup>19,28</sup> indicating that Fe<sub>3</sub>O<sub>4</sub> NPs have been introduced on the MoS<sub>2</sub> to cause the formation of MMoS<sub>2</sub>. After binding of PAA on the MMoS<sub>2</sub>, the typical peak of C=O stretching vibration of PAA at 1716 cm<sup>-1</sup> is evidently observed in all the spectra of MMoS<sub>2</sub>/PAA samples.<sup>20</sup> Besides, the peak of Fe–O is observed to shift from 534 to 555 cm<sup>-1</sup> for both MMoS<sub>2</sub>/PAA-20 and MMoS<sub>2</sub>/PAA-40 with low binding amount of PAA, and shift to 573 cm<sup>-1</sup> for MMoS<sub>2</sub>/PAA-80 and MMoS<sub>2</sub>/PAA-100 with higher binding amount due to the coordination interaction between iron cations and multiple –COO<sup>-</sup> groups.<sup>29</sup> These results indicate that PAA functional molecules and Fe<sub>3</sub>O<sub>4</sub> NPs have successfully introduced on the MoS<sub>2</sub> surface, causing the formation of MMoS<sub>2</sub>/PAA.

The binding amount of PAA on the MMoS<sub>2</sub> surface was estimated by TGA technique. Fig. 1g shows the TGA curves of MMoS<sub>2</sub>, MMoS<sub>2</sub>/PAA-20, MMoS<sub>2</sub>/PAA-40, MMoS<sub>2</sub>/PAA-80, and MMoS<sub>2</sub>/PAA-100. As observed, all the samples exhibited a two-step loss weight process as the temperature increased from 30 to 700 °C. The first weight loss at temperature below ~120 °C was caused by the evaporation of physically-adsorbed water on the materials. The second weight loss at temperature range of 120–430 °C was ascribed to the decomposition of PAA bound on the MoS<sub>2</sub> surface,<sup>20</sup> and the binding amount increased with an increase in PAA dosage during the solvothermal reaction, in agreement with the FT-IR results. The binding amounts were calculated to be respectively 72.9, 156.4, 176.5, and 183.3 mg g<sup>-1</sup> for MMoS<sub>2</sub>/PAA-20, MMoS<sub>2</sub>/PAA-40, MMoS<sub>2</sub>/PAA-80, and MMoS<sub>2</sub>/PAA-100 based on the TGA results. Compared with MMoS<sub>2</sub>/PAA-80, no evident increase of binding amount was observed for MMoS<sub>2</sub>/PAA-100. Therefore, MMoS<sub>2</sub>/PAA-80 was used for the subsequent characterization.

To further characterize the chemical compositions of the MoS<sub>2</sub> before and after modification, the resulted MoS<sub>2</sub> and MMoS<sub>2</sub>/PAA-80 samples were examined by XPS. The high-resolution XPS spectra of Mo 3d and S 2p in MoS<sub>2</sub> and MMoS<sub>2</sub>/PAA-80 were shown in Fig. S1.† The distinct doublet peaks of Mo 3d spectra at 228.6 (Mo 3d<sub>5/2</sub>) and 231.7 eV (Mo 3d<sub>3/2</sub>) were attributed to the Mo<sup>4+</sup> oxidation state of MoS<sub>2</sub> nanosheets<sup>11,30</sup> (Fig. S1a†). The relatively weak peak located at 235.95 eV were assigned to Mo 3d peaks with a higher oxidation state (Mo<sup>6+</sup>), which may originate from the partial oxidation of Mo atoms at the edges or defects on the crystal plane of the MoS<sub>2</sub> nanosheets. The peak located at 225.85 eV was arising from S 2s in MoS<sub>2</sub>, and the two peaks at 162.5 and 161.45 eV were attributed to S 2p<sub>3/2</sub> and S 2p<sub>1/2</sub> (ref. 11 and 30) (Fig. S1c†). After PAA decoration, the corresponding peaks slightly shift towards the higher binding energy (Fig. S1b and d†). Excellent

magnetic property of nanocomposites endows them convenient separability from polluted aqueous solutions under an EMF.

The magnetism of  $\text{MMoS}_2$  before and after PAA modification were studied by VSM. As observed in Fig. 1h, the  $\text{MMoS}_2$  sample had high saturation magnetization ( $M_s$ ) value of  $26.8 \text{ emu g}^{-1}$ . After introduction of non-magnetic PAA on its surface, the  $M_s$  value lowered to  $9.2 \text{ emu g}^{-1}$ . But such a  $M_s$  value was high enough to enable it excellent separability in a few minutes from water under an EMF (Fig. 1h, the right inset). As the EMF was removed, being slightly shaken, the particles could be well redispersed in water, indicating excellent superparamagnetism of the nanocomposite, highly beneficial to its practical application such as dye adsorption.

### 3.2 Adsorption performance

To confirm that PAA bound on the  $\text{MMoS}_2$  played a crucial role in improving the adsorption of cationic dyes, the  $\text{MMoS}_2/\text{PAA}$  serials nanocomposites with various binding amounts of PAA (0, 72.9, 156.4, 176.5, and  $183.3 \text{ mg g}^{-1}$  corresponding to the  $\text{MMoS}_2$ ,  $\text{MMoS}_2/\text{PAA-20}$ ,  $\text{MMoS}_2/\text{PAA-40}$ ,  $\text{MMoS}_2/\text{PAA-80}$ , and  $\text{MMoS}_2/\text{PAA-100}$ ) were utilized to remove three typical dyes of BF, MB and CV from aqueous solutions. Furthermore, in order to prove that  $\text{MoS}_2$  nanosheets played an important role in enhancing the dye adsorption since which provided large

specific surface area for PAA binding and loading of magnetic  $\text{Fe}_3\text{O}_4$  NPs, we carried out an adsorption experiment by using the PAA-bound  $\text{Fe}_3\text{O}_4$  NPs without  $\text{MoS}_2$  components ( $\text{Fe}_3\text{O}_4/\text{PAA-100}$ ) in the nanocomposite. As observed in Fig. 2a, the  $\text{Fe}_3\text{O}_4/\text{PAA-100}$  showed very low adsorption capacities for three cationic dyes. The maximum adsorption capacities of BF, MB, and CV were only  $31.0$ ,  $26.9$ , and  $19.8 \text{ mg g}^{-1}$ , respectively (Fig. 2a). However, when  $\text{Fe}_3\text{O}_4$  NPs were loaded on the  $\text{MoS}_2$  surface to produce  $\text{MMoS}_2$ , which showed higher adsorption capacities for BF, MB, and CV ( $156.78$ ,  $73.15$ , and  $55.33 \text{ mg g}^{-1}$ , respectively) than  $\text{Fe}_3\text{O}_4/\text{PAA-100}$  and the PSSMA-modified  $\text{Fe}_3\text{O}_4$  NPs ( $52.22 \text{ mg g}^{-1}$  for MB) developed in our previous work,<sup>19</sup> indicating that the presence of  $\text{MoS}_2$  with larger specific surface area in the nanocomposite played a crucial role in improving the dye adsorption. Electrostatic interaction between cationic dyes and few numbers of residual anionic groups ( $\text{COO}^-$ ) on the material contributed small adsorption,<sup>20,28</sup> which were generated from incomplete reduction of  $-\text{COOH}$  groups on the surface during the solvothermal process.<sup>20</sup> In comparison to  $\text{MMoS}_2$ , the PAA-bound  $\text{MMoS}_2/\text{PAA}$  serials exhibited much higher dye uptakes since a large number of active sites ( $\text{COO}^-$ ) in PAA available for capturing cationic dye molecules.<sup>20,28</sup> Due to presence of numerous PAA functional molecules on the  $\text{MMoS}_2$ , the  $\text{MMoS}_2/\text{PAA-80}$  behaved long-term water dispersibility

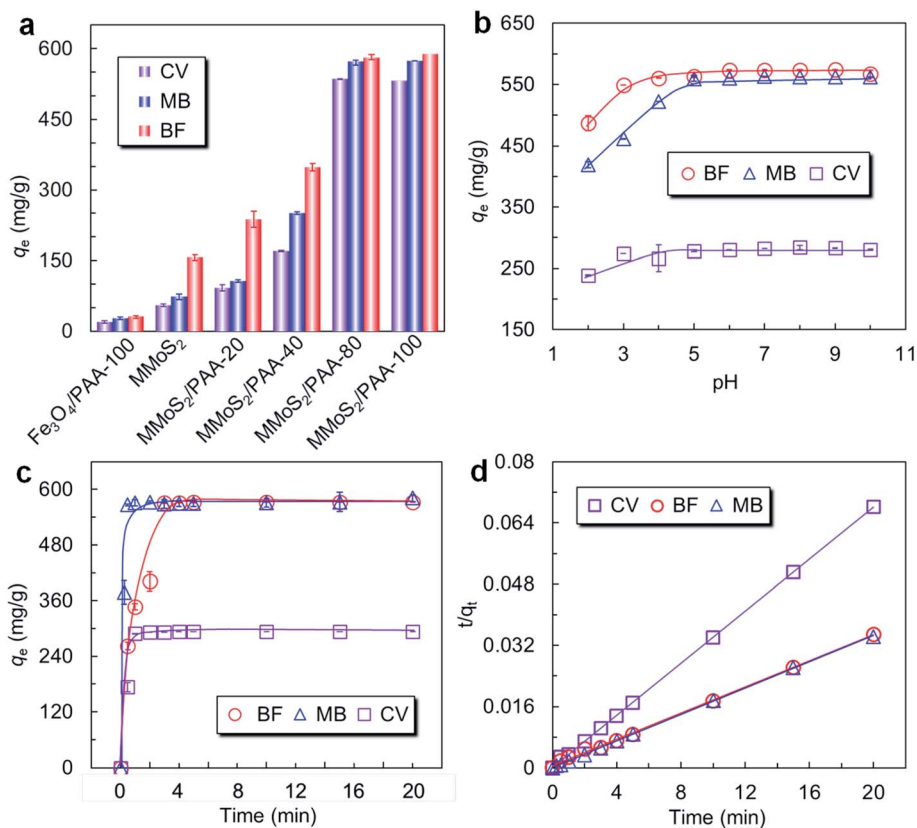


Fig. 2 (a) Equilibrium adsorption capacities of BF, MB, and CV onto  $\text{Fe}_3\text{O}_4/\text{PAA-100}$  and the  $\text{MMoS}_2/\text{PAA}$  serials adsorbents; effects of initial solution pH values (b) and contact time (c) on the adsorption of BF, MB, and CV onto  $\text{MMoS}_2/\text{PAA-80}$ ; (d) fitting curves of pseudo-second-order kinetic model. Condition:  $m/V = 10 \text{ mg}/30 \text{ mL}$ ,  $T = 25^\circ\text{C}$ .  $C_{\text{BF}} = C_{\text{MB}} = C_{\text{CV}} = 200 \text{ mg L}^{-1}$  in (a), and  $C_{\text{CV}} = 100 \text{ mg L}^{-1}$ ,  $C_{\text{BF}} = C_{\text{MB}} = 200 \text{ mg L}^{-1}$  in (b–d).

(Fig. S2a†). By comparison, owing to absence of PAA on the surface,  $\text{MMoS}_2$  particles were easily precipitated out of water within 5 min (Fig. S2b†). Moreover, the uptake of three dyes onto the  $\text{MMoS}_2/\text{PAA}$  increased with increasing PAA dosage during the solvothermal process, and kept nearly invariable at dosage over 80 mg. A larger dosage gave rise to a higher binding amount, thus providing more active sites ( $\text{COO}^-$  groups) for dye adsorption *via* electrostatic interaction, finally leading to higher dye uptakes. Maximum uptakes of BF, MB, and CV onto  $\text{MMoS}_2/\text{PAA-80}$  were respectively 588.0, 574.6, and 535.6  $\text{mg g}^{-1}$  at an initial concentration of 200  $\text{mg L}^{-1}$ , much higher than those on the  $\text{MMoS}_2$ , indicating that PAA polymers on the  $\text{MMoS}_2$  could significantly improve the uptakes of cationic dyes.

**3.2.1 Effect of pH.** Solution pH significantly affects the surface charges of an adsorbent and the degree of ionization of active sites.<sup>10,22</sup> Therefore, effect of solution pH on the adsorption of BF, MB and CV onto  $\text{MMoS}_2/\text{PAA-80}$  was studied in this work. As shown in Fig. 2b, the adsorption capacities of  $\text{MMoS}_2/\text{PAA-80}$  for three dyes were pH-dependent. With increasing solution pH values from 2.0 to 5.0, the uptakes of three dyes increased gradually, and then reached equilibrium at solution pH values above 5.0. Changing solution pH over the investigated range of 2.0–10.0 dramatically affected the surface charges of the synthesized  $\text{MMoS}_2/\text{PAA-80}$  (Fig. S3†), thus the electrostatic interaction between the cationic BF, MB and CV molecules and the negatively charged adsorbent surface, finally their dye uptakes. As the solution pH was lower than 5.0 (nearly the  $\text{pK}_a$  of PAA, 4.75), protonation of  $-\text{COOH}$  groups in PAA molecules weakened the electrostatic interaction between dye molecules and PAA, thus lowering the dye uptakes. While at higher pH media ( $\geq 5.0$ ), deprotonation of  $-\text{COOH}$  increased the surface charges of the  $\text{MMoS}_2/\text{PAA-80}$  (Fig. S3†), thus enhancing the electrostatic interaction between dye molecules and PAA, as a result, promoting dye adsorption.<sup>20,31</sup> Moreover,  $\text{MMoS}_2/\text{PAA-80}$  showed higher uptakes for BF and MB than that for CV due to different initial concentrations of dyes. The initial concentrations of BF, MB and CV were 200, 200 and 100  $\text{mg L}^{-1}$ , respectively. A higher initial concentration facilitated a stronger driving force to overcome the mass transfer resistance of dye molecules between the aqueous phase and the solid phase, thus causing more collisions between dyes and active sites.<sup>32</sup> Since the dye adsorptions were little unchanged at higher pH, the solution pH was fixed at 7.0 in following adsorption experiments.

**3.2.2 Effect of contact time and adsorption kinetics.** The time-dependent dye adsorption onto  $\text{MMoS}_2/\text{PAA-80}$  was

studied at initial concentrations of BF, MB and CV of 200, 200 and 100  $\text{mg L}^{-1}$ , respectively. As observed in Fig. 2c, the adsorption capacities of three dyes onto  $\text{MMoS}_2/\text{PAA-80}$  sharply increased within the first 2 min, and then reached equilibrium. At the first adsorption stage, all the vacant active sites on the  $\text{MMoS}_2/\text{PAA-80}$  were conveniently available for binding dye molecules. As the adsorption proceeded the available number of active sites reduced, and repulsion occurred between the adsorbent and dye molecules. Finally, the equilibrium reached as the adsorption/desorption rates were identical, and increased in adsorption capacities were no longer observed.<sup>10</sup>  $\text{MMoS}_2/\text{PAA-80}$  showed high adsorption capacities for BF, MB and CV (572.1, 581.6, and 293.2  $\text{mg g}^{-1}$ , respectively) due to high binding amounts of PAA on the surface, thus providing plentiful of active sites. This indicates that the synthesized  $\text{MMoS}_2/\text{PAA}$  in this work can serve as an excellent adsorbent for effective removal of cationic dyes from contaminated water. To well understand the adsorption process, two classical kinetic models of pseudo-first-order (eqn (3)) and pseudo-second-order (eqn (4)) kinetic models were used to analyze the adsorption data.

Pseudo-first-order model:<sup>33</sup>

$$\ln(q_e - q_t) = \ln q_e - k_1 t \quad (3)$$

Pseudo-second-order model:<sup>34</sup>

$$\frac{t}{q_1} = \frac{1}{k_2 q_e^2} - \frac{1}{q_e} \quad (4)$$

where  $q_e$  and  $q_t$  ( $\text{mg g}^{-1}$ ) refer to the adsorption capacities of dyes at equilibrium state and at time  $t$  (min), respectively;  $k_1$  ( $\text{min}^{-1}$ ) and  $k_2$  ( $\text{g} (\text{mg}^{-1} \text{min}^{-1})$ ) represent the rate constants of the pseudo-first-order and pseudo-second-order kinetic models, respectively. The values of  $q_e$  and  $k_1$  for pseudo-first-order model could be determined experimentally by plotting  $\ln(q_e - q_t)$  versus  $t$  and extracting information from the least squares analysis of slope and intercept and substituting into eqn (3), while the values of  $q_e$  and  $k_2$  for pseudo-second-order model could be calculated from the slope and intercept of the linear relationship between  $(t/q_t)$  and  $t$  (eqn (4)).

The corresponding kinetic parameters and correlation coefficients ( $R^2$ ) were calculated by the linear regression of the two kinetic models and listed in Table 2. Higher  $R^2$  values ( $>0.998$ ) were obtained for the pseudo-second-order model, and all of the calculated adsorption capacities ( $q_{e,\text{cal}}$ ) for three dyes were closer to the experimental values ( $q_{e,\text{exp}}$ ), indicating that the kinetics of the dyes adsorption onto  $\text{MMoS}_2/\text{PAA-80}$  fitted better

Table 2 Kinetic parameters of the adsorption of BF, MB, and CV onto  $\text{MMoS}_2/\text{PAA-80}$

Dye	$C_0$ ( $\text{mg L}^{-1}$ )	$q_{e,\text{exp}}$ ( $\text{mg g}^{-1}$ )	Pseudo-first-order			Pseudo-second-order		
			$q_{e,\text{cal}}$ ( $\text{mg g}^{-1}$ )	$R^2$	$k_1$ ( $\text{min}^{-1}$ )	$q_{e,\text{cal}}$ ( $\text{mg g}^{-1}$ )	$R^2$	$k_2$ ( $\text{g} (\text{mg}^{-1} \text{min}^{-1})$ )
BF	200	572.1	112.5	0.6840	0.6422	588.2	0.9980	0.0048
MB	200	581.6	24.5	0.1718	0.0826	588.2	0.9999	0.0029
CV	100	293.2	5.1	0.3508	0.3129	294.1	0.9998	0.0578

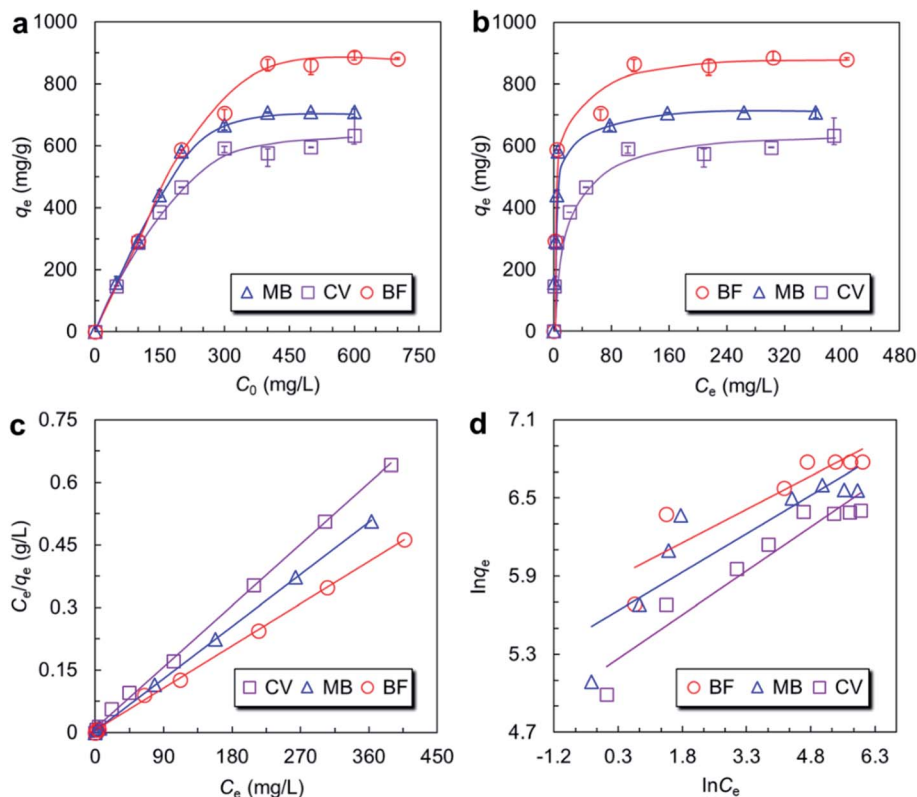


Fig. 3 (a) Effects of initial dye concentrations on the adsorption of BF, MB, and CV onto MMoS<sub>2</sub>/PAA-80; The non-linear regression (b), linear Langmuir (c) and Freundlich (d) isotherms. Condition: pH = 7.0,  $m/V = 10$  mg/30 mL,  $T = 25$  °C, and contact time = 5 min.

the pseudo-second-order model (Fig. 2d and S4<sup>†</sup>), and the interaction between dye molecules and the MMoS<sub>2</sub>/PAA-80 was mainly controlled by chemisorption.

**3.2.3 Effect of initial dye concentrations and adsorption isotherms.** To further study the behaviors of equilibrium adsorption, effect of initial dye concentrations on the adsorption of BF, MB and CV onto MMoS<sub>2</sub>/PAA-80 were also investigated in this work. As shown in Fig. 3a, the adsorption capacities of three dyes gradually increased with increasing the dye concentrations at first, and then reached adsorption saturation at higher concentrations. For a given adsorbent, the total number of active sites ( $-\text{COO}^-$ ) available for binding dye molecules was fixed. At low dye concentrations (below  $400 \text{ mg L}^{-1}$ ), the available active sites on the adsorbent were excessive and could fully interact with relatively insufficient dye molecules in solution *via* strong electrostatic interaction. While at higher concentrations ( $\geq 400 \text{ mg L}^{-1}$ ), dyes became surplus, and those excessive dye molecules were never captured by  $-\text{COO}^-$  groups, thus equilibrium adsorptions were achieved.<sup>35</sup> Moreover, MMoS<sub>2</sub>/PAA-80 showed different adsorption capacities for three dyes over the studied concentration range due to the different molecular structures of dyes. The higher uptake of BF was maybe due to the hydrogen-bond interaction between the primary amino group ( $-\text{NH}_2$ ) in BF molecules and the  $-\text{COOH}$  groups in PAA, facilitating additional dye adsorption. As for MB and CV, a relative larger molecular structure of CV generated higher steric hindrance than MB (Fig. S5<sup>†</sup>), accounted for a lower dye adsorption.

To further ascertain the adsorption mechanism, adsorption isotherms of BF, MB and CV onto MMoS<sub>2</sub>/PAA-80 were investigated in this work. The adsorption data were fitted by the well-known Langmuir and Freundlich isotherm models.<sup>36,37</sup>

Langmuir isotherm model assumes monolayer adsorption of dye molecules over homogenous adsorbent surface, and all of the active sites being equivalent, which was expressed as follows:<sup>36</sup>

$$\frac{C_e}{q_e} = \frac{1}{q_{\max} K_L} - \frac{C_e}{q_{\max}} \quad (5)$$

here,  $C_e$  ( $\text{mg L}^{-1}$ ) is the equilibrium concentration in dye solutions,  $q_e$  and  $q_{\max}$  ( $\text{mg g}^{-1}$ ) are the equilibrium and maximum adsorption capacities of dyes, respectively,  $K_L$  ( $\text{L mg}^{-1}$ ) represents the Langmuir constant related to the energy of adsorption. The values of  $q_{\max}$  and  $K_L$  could be calculated from the slopes and intercepts of the linear plots of  $C_e/q_e$  versus  $C_e$  (eqn (5)).

One of the essential features of Langmuir isotherm could be described by a separation factor,  $R_L$ , which was defined as follows:<sup>4</sup>

$$R_L = \frac{1}{1 + K_L C_0} \quad (6)$$

From the theory of Langmuir isotherm, the value  $R_L$  indicates the shape of Langmuir isotherm to be either unfavorable ( $R_L > 1$ ), linear ( $R_L = 1$ ), favorable ( $1 > R_L > 0$ ) or irreversible ( $R_L = 0$ ). In this study all the  $R_L$  values lay in between 0 and 1,

Table 3 Isotherm parameters of the adsorption of MB, CV and BF onto MMS<sub>2</sub>/PAA-80

Dye	$q_{\text{exp,cal}}$ (mg g <sup>-1</sup> )	Langmuir				Freundlich		
		$q_{\text{max,cal}}$ (mg g <sup>-1</sup> )	$R^2$	$K_L$ (L mg <sup>-1</sup> )	$R_L$	$n_F$	$K_F$ ((mg <sup>-1/n</sup> L <sup>1/n</sup> )/g)	$R^2$
MB	709.0	714.3	0.9998	0.3256	0.0151	4.792	246.8	0.7374
CV	633.6	625.0	0.9989	0.1684	0.0561	4.789	196.0	0.8845
BF	886.1	909.1	0.9992	0.2444	0.0201	5.824	346.9	0.8058

indicating that the adsorption of three dyes onto MMS<sub>2</sub>/PAA-80 were favorable processes.

Freundlich isotherm model takes the assumption that adsorption occurs on heterogeneous surface without saturation of active sites. The equation was expressed as follows:<sup>37</sup>

$$\ln q_e = \frac{1}{n_F} \ln C_e + \ln K_F \quad (7)$$

where  $q_e$  is the equilibrium adsorption capacities of dyes,  $C_e$  (mg L<sup>-1</sup>) is the equilibrium concentration in dye solutions,  $K_F$  ((mg<sup>-1/n</sup> L<sup>1/n</sup>)/g) and  $1/n_F$  represent an empirical parameters related to the intensity of the adsorption interaction.  $K_F$  and  $1/n_F$  could be achieved from the slopes and intercepts of the linear plots of  $\ln q_e$  versus  $\ln C_e$  (eqn (7)).

The Langmuir and Freundlich isotherms obtained by curve fitting were shown in Fig. 3c and d. The model parameters were listed in Table 3. The  $R^2$  values for all the dyes obtained from the Langmuir model higher ( $\geq 0.998$ ) indicated that the Langmuir isotherm model matched better with the experimental data (Fig. 3c). The  $q_{\text{max,cal}}$  values of BF, MB, and CV were 909.1, 714.3, and 625.0 mg g<sup>-1</sup>, respectively, in accordance with the  $q_{\text{max,exp}}$  values well. Therefore, the adsorption of three dyes was monolayer adsorption and the surface of adsorbents was homogeneous.<sup>4,32</sup> Besides, the maximum adsorption capacities of dyes were higher than those materials reported previously (Table 1),<sup>4,10,11,15,18-23</sup> indicating that the synthesized MMS<sub>2</sub>/PAA in this work could serve as an excellent adsorbent for effective removal of cationic dye wastewater.

**3.2.4 Effect of temperature and thermodynamics of adsorption.** Temperature is another significant factor to be considered during the adsorption of dyes since it affects the adsorption rate which in turn affects the equilibrium adsorption capacity. Fig. S6† showed the effect of temperature on the adsorption of BF, MB and CV onto MMS<sub>2</sub>/PAA-80 at initial concentrations of 200, 200 and 100 mg L<sup>-1</sup>, respectively. The adsorption capacities decreased with increased temperatures.

The thermodynamic parameters reflecting internal energy changes for the adsorption process, including free energy change ( $\Delta G$ ), enthalpy change ( $\Delta H$ ), and entropy change ( $\Delta S$ ), were calculated by the following equations:<sup>22</sup>

$$\Delta G = -RT \ln K_L \quad (8)$$

$$\ln K_L = \frac{\Delta S}{R} - \frac{\Delta H}{RT} \quad (9)$$

where  $R$  is the universal gas constant (8.314 J (mol<sup>-1</sup> K<sup>-1</sup>)),  $T$  is the absolute temperature (K), and  $K_L$  is the Langmuir constant. The values of  $\Delta H$  and  $\Delta S$  were obtained from the slope and intercept of the van't Hoff plot of  $\ln K_L$  versus  $1/T$ .

The  $\Delta G$ ,  $\Delta H$ , and  $\Delta S$  values of three dyes at various temperatures were listed in Table 4. The positive values of  $\Delta S$  indicated the affinity of MMS<sub>2</sub>/PAA-80 for three dyes and increasing randomness at the solid-liquid interface in the adsorption reaction. The negative values of  $\Delta H$  showed that the adsorption processes were exothermic. The negative values of  $\Delta G$  increased with an increase in temperature, indicating that the adsorption was spontaneous and more favorable at lower temperature.<sup>32</sup>

**3.2.5 Adsorption of mixed dyes.** Industrial effluents usually coexists with several dyes. Therefore, the adsorption performances of the synthesized MMS<sub>2</sub>/PAA-80 for mixed dyes were also studied in this work. As observed in Fig. 4a, the MMS<sub>2</sub>/PAA-80 showed high removal efficiencies for various concentration combinations of mixed-dye solutions. With increasing the concentrations of mixed dyes, the removal efficiencies slightly reduced due to that the vacant active sites on the MMS<sub>2</sub>/PAA-80 were saturated by the dye molecules in solutions as the concentration higher than certain value. However, high removal efficiency (>85%) even for the highest combined concentrations ( $C_{\text{MB}} = C_{\text{CV}} = C_{\text{BF}} = 120$  mg L<sup>-1</sup>) indicated a superior adsorption performance of the MMS<sub>2</sub>/PAA-80 for mixed dyes. Moreover, MMS<sub>2</sub>/PAA-80 demonstrated slightly higher removal efficiency of MB than of BF and CV for all the mixed-dye solutions. This was probably owing to that the

Table 4 Thermodynamic parameters for MB, CV and BF adsorption by MMS<sub>2</sub>/PAA-80

$T$ (K)	$\Delta G$ (kJ mol <sup>-1</sup> )			$\Delta H$ (kJ mol <sup>-1</sup> )			$\Delta S$ (J (mol <sup>-1</sup> ·K))		
	MB	CV	BF	MB	CV	BF	MB	CV	BF
298	-11.96	-11.44	-12.30	-124.82	-118.25	-148.70	0.38	0.36	0.46
308	-6.51	-6.14	-5.88						
318	-4.98	-4.51	-3.90						



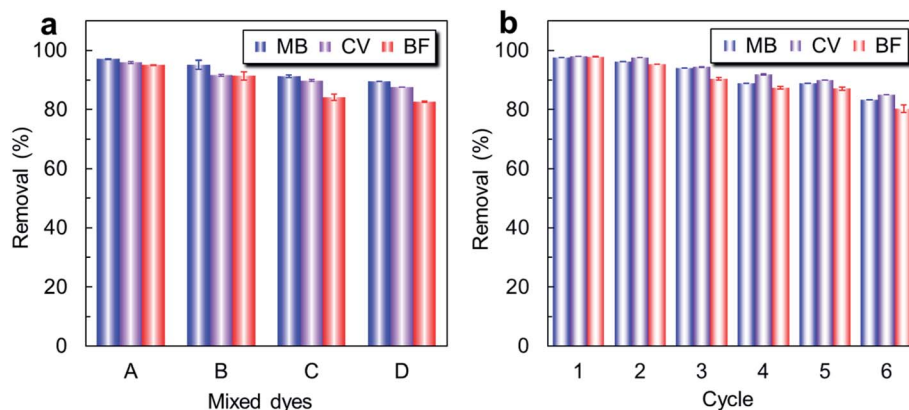


Fig. 4 (a) Removal efficiencies of MB, CV and BF in mixed-dye solutions with various concentration combinations by MMoS<sub>2</sub>/PAA-80. The four concentration combinations of the mixed dye solutions as: sample A:  $C_{MB} = C_{CV} = C_{BF} = 60 \text{ mg L}^{-1}$ , sample B:  $C_{MB} = C_{CV} = C_{BF} = 80 \text{ mg L}^{-1}$ , sample C:  $C_{MB} = C_{CV} = C_{BF} = 100 \text{ mg L}^{-1}$ , sample D:  $C_{MB} = C_{CV} = C_{BF} = 120 \text{ mg L}^{-1}$ . Conditions: pH = 7.0,  $m/V = 10 \text{ mg}/30 \text{ mL}$ ,  $T = 25 \text{ }^\circ\text{C}$  and contact time = 5 min. (b) Reusability of MMoS<sub>2</sub>/PAA-80 for dye removal. Conditions:  $C_{MB} = C_{BF} = 200 \text{ mg L}^{-1}$ ,  $C_{CV} = 100 \text{ mg L}^{-1}$ , pH = 7.0,  $m/V = 10 \text{ mg}/30 \text{ mL}$ ,  $T = 25 \text{ }^\circ\text{C}$  and contact time = 5 min.

adsorption of MB in mixed solutions restricted the adsorption of BF and CV by steric effects or preferential occupation of active sites on the MMoS<sub>2</sub>/PAA-80, resulted from relative larger molecular weights of BF and CV and their distinct structure features (Fig. S5†).

**3.2.6 Regeneration performance.** The regeneration ability of an adsorbent play an important role in its practical application. The loaded Fe<sub>3</sub>O<sub>4</sub> NPs on the MoS<sub>2</sub> nanosheets endowed it excellent separability from polluted water under an EMF (Fig. 1h), therefore, the dye-saturated nanocomposite could be readily recovered and regenerated using NaOH ethanol solutions (0.1 M). The regenerability was evaluated by the removal efficiency of MMoS<sub>2</sub>/PAA-80 for MB, CV and BF in six successive cycles as presented in Fig. 4b. The removal efficiencies of three dyes slightly reduced with increasing the cycles due to the loss of small amount of adsorbent during the washing process. However, over 80% removal efficiency were still achieved even it was suffered from six successive cycles of adsorption/desorption process, indicating that the MMoS<sub>2</sub>/PAA owns excellent regenerability and is promising to serve as an excellent adsorbent for treating cationic dye wastewater.

## 4. Conclusions

In summary, polyacrylic acid (PAA) decorated magnetic MoS<sub>2</sub> nanosheets (MoS<sub>2</sub>/PAA) with high adsorption capacities for three cationic dyes of basic fuchsin (BF), methylene blue (MB), and crystal violet (CV) have been successfully synthesized by a simple solvothermal method. PAA with rich anionic groups (–COOH) played a crucial role in significantly enhancing the dye adsorption. Ultrafast adsorption rate and high adsorption capacities of BF, MB and CV onto MMoS<sub>2</sub>/PAA are mainly driven by strong electrostatic interaction between cationic dyes and the anionic MMoS<sub>2</sub>/PAA surface. The adsorption capacities of three dyes dramatically increased with increasing the binding amount of PAA. The adsorption behaviors of dyes onto MMoS<sub>2</sub>/PAA were well fitted with the pseudo-second-order kinetic and

the Langmuir models. The batch adsorption experiments with the effects of parameters like solution pH, contact time, initial dye concentrations and temperature on the adsorption were optimized for dye adsorption. Moreover, the MMoS<sub>2</sub>/PAA also showed high removal efficiencies for various mixed-dye solutions and excellent regenerability. Such a functional nanocomposite with ultrafast adsorption rate and high adsorption capacities for cationic dyes can serve as an excellent adsorbent for effective removal of variety of cationic contaminants from industrial effluents.

## Conflicts of interest

There are no conflicts to declare.

## Acknowledgements

This work was supported by the National Natural Science Foundation of China (21676219), the Sichuan Science and Technology Program (2019YJ0254), and the Fundamental Research Funds for the Central Universities, Southwest Minzu University (2020PTJS20010).

## Notes and references

- 1 K. M. Lee, C. W. Lai, K. S. Ngai and J. C. Juan, *Water Res.*, 2016, **88**, 428.
- 2 V. Katheresan, J. Kansedo and S. Y. Lau, *J. Environ. Chem. Eng.*, 2018, **6**, 4676.
- 3 E. N. E. Qada, S. J. Allen and G. M. Walker, *Chem. Eng. J.*, 2008, **135**, 174.
- 4 L. Fan, C. Luo, X. Li, F. Lu, H. Qiu and M. Sun, *J. Hazard. Mater.*, 2012, **215–216**, 272.
- 5 K. B. Tan, M. Vakili, B. A. Hord, P. E. Poh, A. Z. Abdullah and B. Salamatinia, *Sep. Purif. Technol.*, 2015, **150**, 229.
- 6 S. Natarajan, H. C. Bajaj and R. J. Tayade, *J. Environ. Sci.*, 2018, **65**, 204.

- 7 M. Rafatullah, O. Sulaiman, R. Hashim and A. Ahmad, *J. Hazard. Mater.*, 2010, **177**, 70.
- 8 K. Lu, G. X. Zhao and X. K. Wang, *Chin. Sci. Bull.*, 2012, **57**, 1223.
- 9 I. Ali, A. A. Basheer, X. Y. Mbianda, A. Burakov, E. Galunin, I. Burakova, E. Mkrtchyan, A. Tkachev and V. Grachev, *Environ. Int.*, 2019, **127**, 160.
- 10 A. Gopalakrishnan, S. P. Singh and S. Badhulika, *New J. Chem.*, 2020, **44**, 5489.
- 11 X. Q. Qiao, F. C. Hu, F. Y. Tian, D. F. Hou and D. S. Li, *RSC Adv.*, 2016, **6**, 11631.
- 12 Z. Y. Wang and B. X. Mi, *Environ. Sci. Technol.*, 2017, **51**, 8229.
- 13 C. Liu, F. F. Jia, Q. M. Wang, B. Q. Yang and S. X. Song, *Appl. Mater. Today*, 2017, **9**, 220.
- 14 S. Yang, M. X. Hua, L. Shen, X. L. Han, M. Y. Xu, L. J. Kuang and D. B. Hua, *J. Hazard. Mater.*, 2018, **354**, 191.
- 15 H. J. Song, S. S. You, X. H. Jia and J. Yang, *Ceram. Int.*, 2015, **41**, 13896.
- 16 A. S. K. Kumar, S. J. Jiang and J. K. Warchoř, *ACS Omega*, 2017, **2**, 6187.
- 17 Y. Chen, B. H. Song, X. S. Tang, L. Lu and J. M. Xue, *Small*, 2014, **10**, 1536.
- 18 T. M. F. Marques, D. A. Sales, L. S. Silva, R. D. S. Bezerra, M. S. Silva, J. A. Osajima, O. P. Ferreira, A. Ghosh, E. C. S. Filho, B. C. Viana and J. M. E. Matos, *Appl. Surf. Sci.*, 2020, **512**, 145659.
- 19 Y. B. Song, S. N. Lv, C. J. Cheng, G. L. Ni, X. W. Xie, W. Huang and Z. G. Zhao, *Appl. Surf. Sci.*, 2015, **324**, 854.
- 20 J. W. Zhang, M. S. Azam, C. Shi, J. Huang, B. Yan, Q. X. Liu and H. B. Zeng, *RSC Adv.*, 2015, **5**, 32272.
- 21 R. Samadder, N. Akter, A. C. Roy, M. M. Uddin, M. J. Hossen and M. S. Azam, *RSC Adv.*, 2020, **10**, 11945.
- 22 X. D. Liu, J. F. Tian, Y. Y. Li, N. F. Sun, S. Mi, Y. Xie and Z. Y. Chen, *J. Hazard. Mater.*, 2019, **373**, 397.
- 23 D. W. Cho, B. H. Jeon, C. M. Chon, F. W. Schwartz, Y. Jeong and H. Song, *J. Ind. Eng. Chem.*, 2015, **28**, 60.
- 24 J. Zhang, J. M. Soon, K. P. Loh, J. Yin, J. Ding, M. B. Sullivan and P. Wu, *Nano Lett.*, 2007, **7**, 2370.
- 25 D. Su, S. Dou and G. Wang, *Adv. Energy Mater.*, 2014, **5**, 1401205.
- 26 A. T. Massey, R. Gusain, S. Kumari and O. P. Khatri, *Ind. Eng. Chem. Res.*, 2016, **55**, 7124.
- 27 N. J. Fu, L. T. Li, K. J. Liu, C. K. Kim, J. Li, T. Zhu, J. H. Li and B. K. Tang, *Talanta*, 2019, **197**, 567.
- 28 Y. Y. Xu, M. Zhou, H. J. Geng, J. J. Hao, Q. Q. Ou, S. D. Qi, H. L. Chen and X. G. Chen, *Appl. Surf. Sci.*, 2012, **258**, 3897.
- 29 W. J. Xu, M. S. Wang, Z. W. Li, X. J. Wang, Y. Q. Wang, M. Y. Xing and Y. D. Yin, *Nano Lett.*, 2017, **17**, 2713.
- 30 Q. W. Wang, S. Y. Dong and D. Zhang, *J. Mater. Sci.*, 2018, **53**, 1135.
- 31 Q. Y. Lv, Y. Shen, Y. Qiu, M. Wu and L. M. Wang, *J. Appl. Polym. Sci.*, 2020, **137**, e49322.
- 32 L. H. Ai, C. Y. Zhang and Z. L. Chen, *J. Hazard. Mater.*, 2011, **192**, 1515.
- 33 S. Largegren, *K. Sven. Vetenskapsakad. Handl.*, 1898, **24**, 1.
- 34 Y. S. Ho and G. M. McKay, *Proc. Biochem.*, 1999, **34**, 451.
- 35 H. Yan, X. Tao, Z. Yang, K. Li, H. Yang, A. M. Li and R. S. Cheng, *J. Hazard. Mater.*, 2014, **268**, 191.
- 36 I. Langmuir, *J. Am. Chem. Soc.*, 1916, **38**, 2221.
- 37 H. M. F. Freundlich, *J. Phys. Chem.*, 1906, **57**, 385.